

Enhanced Privacy Leakage from Noise-Perturbed Gradients via Gradient-Guided Conditional Diffusion Models

Jiayang Meng^{1*}, Tao Huang^{2*}, Hong Chen^{1†}, Chen Hou^{2†}, Guolong Zheng²

¹School of Information, Renmin University of China, Beijing 100872, China

²School of Computer Science and Big Data, Minjiang University, Fuzhou, Fujian 350108, China
 {jiayangmeng, chong}@ruc.edu.cn, {huang-tao, houchen, gzheng}@mju.edu.cn

Abstract

Federated learning synchronizes models through gradient transmission and aggregation. However, these gradients pose significant privacy risks, as sensitive training data is embedded within them. Existing gradient inversion attacks suffer from significantly degraded reconstruction performance when gradients are perturbed by noise—a common defense mechanism. In this paper, we introduce Gradient-Guided Conditional Diffusion Models (GG-CDMs) for reconstructing private images from leaked gradients without prior knowledge of the target data distribution. Our approach leverages the inherent denoising capability of diffusion models to circumvent the partial protection offered by noise perturbation, thereby improving attack performance under such defenses. We further provide a theoretical analysis of the reconstruction error bounds and the convergence properties of attack loss, characterizing the impact of key factors—such as noise magnitude and attacked model architecture—on reconstruction quality. Extensive experiments demonstrate our attack’s superior reconstruction performance with Gaussian noise-perturbed gradients, and confirm our theoretical findings.

1 Introduction

Federated Learning (FL) is a prominent paradigm for collaborative model training, which aggregates locally computed gradients from multiple clients without sharing raw private data (Kairouz et al. 2021; Li et al. 2020). However, gradients inherently encode sensitive training data, making them vulnerable to Gradient Inversion Attacks (GIAs) (Zhu, Liu, and Han 2019; Jeon et al. 2021a; Fang et al. 2023a)—where adversaries aim to recover private training data from leaked gradients. This privacy risk is especially critical in sensitive domains such as medical imaging and biometric authentication, where private training data is highly valuable and costly to acquire, making it an attractive target for adversaries.

Existing GIAs based on pixel-space differentiation (Zhu, Liu, and Han 2019; Zhao, Mopuri, and Bilen 2020; Geiping et al. 2020a) struggle with high-resolution images, as iterative differentiation of a randomly initialized image becomes computationally prohibitive at higher resolutions.

*These authors contributed equally.

†Corresponding authors: Hong Chen and Chen Hou.

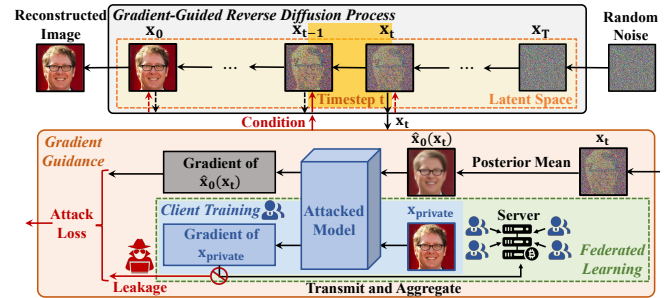


Figure 1: An overview of our proposed gradient-guided conditional diffusion model.

GIAs leveraging generative models, such as Generative Adversarial Networks (GANs) and diffusion models, require an additional assumption that the generative model’s pre-training data distribution aligns with that of the target images. Furthermore, GAN-based GIAs (Yin et al. 2021a; Jeon et al. 2021b; Li et al. 2022a; Fang et al. 2023b) often suffer from model collapse and training instability, resulting in blurry or artifact-ridden reconstructions. Diffusion model-based GIAs (Ho, Jain, and Abbeel 2020a; Song and Ermon 2019; Song et al. 2020; Meng et al. 2024), which typically rely on model fine-tuning, inherently struggle to precisely recover image details due to the lack of pixel-level guidance.

To mitigate privacy risks associated with gradient leakage, a common strategy is to perturb gradients with noise (e.g., Gaussian or Laplacian) before transmission (Geiping et al. 2020b; Yin et al. 2021b; Li et al. 2022b; Jeon et al. 2021a; Fang et al. 2023a). Empirical studies (Meng et al. 2024; Wang et al. 2022; El Mestari, Lenzini, and Demirci 2024) confirm that this noise injection effectively mitigates GIAs, significantly degrading GIA performance when reconstructing training data from these noise-perturbed gradients.

In this paper, we explore how the inherent denoising capability of diffusion models can be leveraged to partially circumvent the protection offered by perturbed noise, as illustrated in Figure 1, thereby improving attack performance. Specifically, our contributions are summarized as follows.

- We propose a novel method for pixel-level, prior-free reconstruction of high-resolution private images from noise-perturbed gradients. Our attack leverages gradient-

guided conditional diffusion models and requires minimal modifications to standard reverse diffusion sampling.

- Theoretically, we derive reconstruction error bounds and characterize the convergence properties of the attack loss. Our analysis rigorously quantifies how noise scale and attacked model architecture affect reconstruction quality.
- We conducted extensive experiments to validate the effectiveness of our proposed GIA method, with results consistently supporting our theoretical findings.

2 Related Work

2.1 Pixel-Space Differentiation-Based GIAs

Gradient inversion attacks (GIAs) based on pixel-space differentiation (Zhu, Liu, and Han 2019; Zhao, Mopuri, and Bilen 2020; Geiping et al. 2020a) typically initialize a differentiable dummy image and iteratively update it by minimizing an attack loss function. Specifically, (Zhu, Liu, and Han 2019; Zhao, Mopuri, and Bilen 2020) minimize the Mean Squared Error (MSE) for pixel-wise accuracy. (Geiping et al. 2020a) improves reconstruction fidelity by introducing a carefully designed attack loss function. However, these approaches face significant scalability challenges when reconstructing high-resolution images, due to the inherent computational complexity of differentiation. Furthermore, their performance is severely degraded when the leaked gradients are perturbed by noise, as the target image, which corresponds to these noise-perturbed gradients, is distorted.

2.2 Generative Model-Based GIAs

Recent advances leverage generative models for high-resolution image reconstruction, addressing the computational complexity of differentiation-based methods. Specifically, (Yin et al. 2021a; Jeon et al. 2021b; Li et al. 2022a; Fang et al. 2023b) have demonstrated that Generative Adversarial Networks (GANs) can serve as effective priors by approximating the natural image manifold, thus improving GIA performance. However, GAN-based methods require distributional alignment between the target image and the GAN’s training set, and they often suffer from training instability. Diffusion models provide a promising alternative, with (Meng et al. 2024) demonstrating that model fine-tuning enables stable and noise-free image reconstruction. Nevertheless, this fine-tuning paradigm suffers from several limitations: high computational cost due to its iterative nature, reliance on the distributional prior of target data, model overfitting that degrades generation quality, and the absence of pixel-level guidance for fine-grained detail recovery.

3 Preliminaries

3.1 Diffusion Models

Diffusion models (Nichol and Dhariwal 2021; Rombach et al. 2022), inspired by the physical process of diffusion, are a class of generative models capable of producing high-quality and diverse samples. In the forward diffusion process, diffusion models gradually perturb clean data $\mathbf{x}_0 \sim p_{\text{data}}$ by adding Gaussian noise until it becomes pure noise. In both DDPM (Ho, Jain, and Abbeel 2020b) and DDIM

(Song, Meng, and Ermon 2020), the posterior distribution of any $\mathbf{x}_t, t \in [0, T]$ given \mathbf{x}_0 is defined as:

$$\mathbf{x}_t = \sqrt{\alpha_t} \mathbf{x}_0 + \sqrt{1 - \alpha_t} \epsilon_t, \epsilon_t \sim \mathcal{N}(0, I). \quad (1)$$

Here, $\{\bar{\alpha}_t\}_{t=0}^T$ is the pre-defined noise schedule. The objective is to train a Denoiser, $\epsilon_\theta(\mathbf{x}_t, t)$, to predict the noise ϵ_t added at each timestep t . This is achieved by minimizing the expected discrepancy between the true and predicted noise:

$$L_{\text{Denoiser}} = \mathbb{E}_{t, \mathbf{x}_0, \epsilon_t} [\|\epsilon_t - \epsilon_\theta(\mathbf{x}_t, t)\|^2]. \quad (2)$$

During the reverse diffusion process, the joint distribution $p(\mathbf{x}_{0:T})$ can be defined as:

$$p(\mathbf{x}_{0:T}) = p(\mathbf{x}_T) \prod_{t=1}^T p_\theta(\mathbf{x}_{t-1} | \mathbf{x}_t), \quad (3)$$

$$p_\theta(\mathbf{x}_{t-1} | \mathbf{x}_t) = \mathcal{N}(\mathbf{x}_{t-1}; \mu_\theta(\mathbf{x}_t, t), \Sigma_\theta(\mathbf{x}_t, t)). \quad (4)$$

In our attack, we employ the reverse sampling of DDIM:

$$\begin{aligned} \mathbf{x}_{t-1} = & \underbrace{\sqrt{\alpha_{t-1}} \left(\frac{\mathbf{x}_t - \sqrt{1 - \alpha_t} \epsilon_\theta(\mathbf{x}_t, t)}{\sqrt{\alpha_t}} \right)}_{\text{predicted } \mathbf{x}_0} \\ & + \underbrace{\sqrt{1 - \alpha_{t-1} - \sigma_t^2} \cdot \epsilon_\theta(\mathbf{x}_t, t)}_{\text{direction pointing to } \mathbf{x}_t} + \underbrace{\sigma_t \epsilon_t}_{\text{random noise}}, \end{aligned} \quad (5)$$

where $\sigma_t = \eta \sqrt{\frac{1 - \alpha_{t-1}}{1 - \alpha_t}} \sqrt{1 - \frac{\alpha_t}{\alpha_{t-1}}}$ and $\epsilon_t \sim \mathcal{N}(0, I)$.

3.2 Conditional Diffusion Models

Conditional diffusion models (Dhariwal and Nichol 2021; Ho and Salimans 2022; Chung et al. 2022c; Yu et al. 2023; He et al. 2023; Yang et al. 2024) incorporate a given condition or measurement \mathbf{y} by introducing an additional likelihood term $p(\mathbf{x}_t | \mathbf{y})$. According to Bayes’ rule,

$$\nabla_{\mathbf{x}_t} \log p(\mathbf{x}_t | \mathbf{y}) = \nabla_{\mathbf{x}_t} \log p(\mathbf{x}_t) + \nabla_{\mathbf{x}_t} \log p(\mathbf{y} | \mathbf{x}_t). \quad (6)$$

With DDIM as the prior, the term $\nabla_{\mathbf{x}_t} \log p(\mathbf{y} | \mathbf{x}_t)$ can be utilized to perform an additional correction step:

$$\mathbf{x}_{t-1} = \underbrace{\text{DDIM}(\mathbf{x}_t, \epsilon_\theta(\mathbf{x}_t, t))}_{\text{sampling step}} - \underbrace{\gamma \nabla_{\mathbf{x}_t} \log p(\mathbf{y} | \mathbf{x}_t)}_{\text{conditional correction step}}. \quad (7)$$

4 Methodology

4.1 Problem Statement

In FL, consider a client-side model $F(\mathbf{x}; W)$ parameterized by W under attack. For a given private image $\mathbf{x}_{\text{private}} \in \mathbb{X}$, the corresponding gradient of $F(\mathbf{x}; W)$ is:

$$\mathbf{g}(\mathbf{x}_{\text{private}}) = \nabla_W F(\mathbf{x}_{\text{private}}; W). \quad (8)$$

In the context of Gaussian noise-based defenses for gradient protection, the perturbed gradient can be expressed as $\mathbf{g}_{\text{leaked}} = \mathbf{g}(\mathbf{x}_{\text{private}}) + \mathcal{N}(0, \sigma^2 I) = \mathcal{N}(\mathbf{g}(\mathbf{x}_{\text{private}}), \sigma^2 I)$, which follows a Gaussian distribution. Given leaked gradient $\mathbf{g}_{\text{leaked}}$, access to the attacked model F (which allows gradient computation for arbitrary inputs), and a diffusion model $\epsilon_\theta(\mathbf{x})$ pre-trained on an arbitrary dataset without requirement of distributional alignment with $\mathbf{x}_{\text{private}}$, the objective is to generate an image \mathbf{x} such that $\mathbf{g}(\mathbf{x})$ approximates $\mathbf{g}(\mathbf{x}_{\text{private}})$, thereby ensuring \mathbf{x} approximates $\mathbf{x}_{\text{private}}$.

4.2 Posterior Distribution Approximation

To enable computationally efficient, fine-grained, and pixel-level reconstruction through a single reverse diffusion process, we use the leaked gradients as a conditioning signal to guide diffusion model’s reverse steps. A key challenge in constructing this model lies in deriving $p(\mathbf{y} = \mathbf{g}_{\text{leaked}} | \mathbf{x}_t)$ in Equation (7), due to the time-dependent nature of \mathbf{x}_t . A tractable approximation can be factorized as:

$$p(\mathbf{y} = \mathbf{g}_{\text{leaked}} | \mathbf{x}_t) = \int p(\mathbf{y} = \mathbf{g}_{\text{leaked}} | \mathbf{x}_0) p(\mathbf{x}_0 | \mathbf{x}_t) d\mathbf{x}_0. \quad (9)$$

From the DDIM forward diffusion process (Equation (1)), the posterior mean $\hat{\mathbf{x}}_0$ conditioned on \mathbf{x}_t can be obtained as:

$$\begin{aligned} \hat{\mathbf{x}}_0(\mathbf{x}_t) &:= \mathbb{E}[\mathbf{x}_0 | \mathbf{x}_t] = \mathbb{E}_{\mathbf{x}_0 \sim p(\mathbf{x}_0 | \mathbf{x}_t)}[\mathbf{x}_0] \\ &= \frac{1}{\sqrt{\alpha_t}} (\mathbf{x}_t - (1 - \alpha_t) \epsilon_\theta(\mathbf{x}_t, t)). \end{aligned} \quad (10)$$

We then approximate:

$$p(\mathbf{g}_{\text{leaked}} | \mathbf{x}_t) \simeq p(\mathbf{g}_{\text{leaked}} | \hat{\mathbf{x}}_0(\mathbf{x}_t)). \quad (11)$$

The error induced by the posterior mean approximation is naturally quantified by the Jensen gap.

Definition 4.1 (Jensen Gap (Chung et al. 2022a)). Let \mathbf{x} be a random variable with distribution $p(\mathbf{x})$. For some function f that may or may not be convex, Jensen gap is defined as:

$$\mathcal{J}(f, \mathbf{x} \sim p(\mathbf{x})) = \mathbb{E}[f(\mathbf{x})] - f(\mathbb{E}[\mathbf{x}]), \quad (12)$$

where the expectation is taken over $p(\mathbf{x})$.

Specifically, the approximation error can be expressed as $\mathbb{E}_{\mathbf{x}_0 | \mathbf{x}_t} [f(\mathbf{x}_0)] - f(\mathbb{E}[\mathbf{x}_0 | \mathbf{x}_t])$, where f is a function such as gradient computation. A smaller Jensen gap implies a lower approximation error and thus higher reconstruction fidelity.

4.3 Attack Methodology

In this section, we propose *Gaussian Spherical Sampling-Reconstruction (GSS-R)*, a novel GIA method that leverages Gradient-Guided Conditional Diffusion Models (GG-CDMs) to reconstruct private training images from leaked gradients via a single reverse diffusion process.

We first introduce a symmetric and differentiable attack loss function $\mathcal{L}(\cdot, \cdot) = \|\cdot - \cdot\|$, which satisfies $\mathcal{L}(a, b) = \mathcal{L}(b, a)$. Conditioned on the leaked gradient $\mathbf{g}_{\text{leaked}}$, the reverse sampling process at timestep t is formulated as:

$$\arg \min_{\mathbf{x}_{t-1}} [\nabla_{\mathbf{x}_t} \mathcal{L}(\mathbf{g}(\hat{\mathbf{x}}_0(\mathbf{x}_t)), \mathbf{g}_{\text{leaked}})]^T (\mathbf{x}_{t-1} - \mathbf{x}_t), \quad (13)$$

where $\mathbf{x}_{t-1} \in CI_{1-\delta}$, with $CI_{1-\delta}$ denoting the $1 - \delta$ confidence intervals for the Gaussian distribution defined in Equation (4). This constrained optimization aims to steer the reverse sampling toward directions that most rapidly minimize the attack loss while enforcing sampling within high-confidence intervals under the DDIM Gaussian distribution.

Due to the high-dimensional nature of gradients, direct optimization is challenging. Previous theoretical work (Ledoux 2001) has established that Gaussian-distributed variables exhibit concentration around their mean. The Laurent-Massart bound (Laurent and Massart 2000) further provides bounds on the deviation of a Gaussian variable from its mean, as formalized in Lemma 4.1.

Lemma 4.1 (Laurent-Massart Bound (Laurent and Massart 2000)). For an n -dimensional isotropy Gaussian distribution $\mathbf{x} \sim \mathcal{N}(\mu, \sigma^2 I)$, it satisfies:

$$P(\|\mathbf{x} - \mu\|^2 \geq n\sigma^2 + 2n\sigma^2(\sqrt{\epsilon} + \epsilon)) \leq e^{-n\epsilon}, \quad (14)$$

$$P(\|\mathbf{x} - \mu\|^2 \leq n\sigma^2 + 2n\sigma^2\sqrt{\epsilon}) \leq e^{-n\epsilon}, \quad (15)$$

where n is \mathbf{x} ’s dimension.

When n is large, $e^{-n\epsilon}$ approaches 0. In this case, \mathbf{x} is distributed on a sphere with radius $\sqrt{n}\sigma$ centered at μ . The distribution of \mathbf{x} follows: $\mathbf{x} \sim S_{\mu_\theta(\mathbf{x}_t, t), \sqrt{n}\sigma_t}^n = \{\mathbf{x} \in \mathbb{R}^n, \|\mathbf{x} - \mu_\theta(\mathbf{x}_t, t)\| = \sqrt{n}\sigma_t\}$. With this spherical constraint, the optimization problem has a closed-form solution:

$$\mathbf{x}_{t-1}^* = \mu_\theta(\mathbf{x}_t, t) - \sqrt{n}\sigma_t \frac{\nabla_{\mathbf{x}_t} \mathcal{L}(\mathbf{g}(\hat{\mathbf{x}}_0(\mathbf{x}_t)), \mathbf{g}_{\text{leaked}})}{\|\nabla_{\mathbf{x}_t} \mathcal{L}(\mathbf{g}(\hat{\mathbf{x}}_0(\mathbf{x}_t)), \mathbf{g}_{\text{leaked}})\|}. \quad (16)$$

We term this conditional sampling as Gaussian Spherical Sampling (GSS). Figure 2 provides an intuitive illustration of GSS at timestep t , and Algorithm 1 outlines the GSS-R.

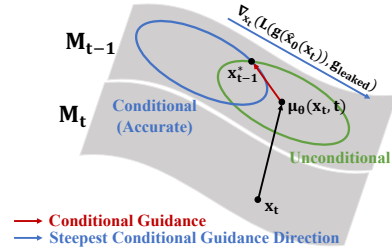


Figure 2: An overview of GSS at timestep t , mapping from data manifold M_t to M_{t-1} . The green annulus represents the concentration region of samples in unconditional DDIM reverse sampling, and the blue annulus denotes the concentration region under accurate conditional guidance.

Algorithm 1: Gaussian Spherical Sampling-Reconstruction.

Input: Pre-trained diffusion model ϵ_θ with maximum timestep T ; Pre-defined noise schedule $\{\alpha_t\}_{t=1}^T$ and denoising scale $\{\sigma_t\}_{t=1}^T$; Attacked model $F(\mathbf{x}; W)$ where $\mathbf{x} \in \mathbb{R}^n$; Leaked gradient $\mathbf{g}_{\text{leaked}}$; Attack loss function \mathcal{L} .

Output: Reconstructed Image \mathbf{x}_0 .

- 1: Randomly initialize a dummy image: $\mathbf{x}_T \sim \mathcal{N}(0, I)$.
- 2: **for** $t = T$ to 1 **do**
- 3: Predict added noise at forward step t : $\hat{\epsilon}_t \leftarrow \epsilon_\theta(\mathbf{x}_t, t)$.
- 4: Approximate the posterior mean:
 $\hat{\mathbf{x}}_0(\mathbf{x}_t) \leftarrow \frac{1}{\sqrt{\alpha_t}} (\mathbf{x}_t - (1 - \alpha_t) \hat{\epsilon}_t)$.
- 5: Compute the mean of \mathbf{x}_{t-1} :
 $\mu_\theta(\mathbf{x}_t, t) = \sqrt{\alpha_{t-1}} \hat{\mathbf{x}}_0(\mathbf{x}_t) + \sqrt{1 - \alpha_{t-1} - \sigma_t^2} \cdot \hat{\epsilon}_t$.
- 6: Input $\hat{\mathbf{x}}_0(\mathbf{x}_t)$ to F to calculate $\mathbf{g}(\hat{\mathbf{x}}_0(\mathbf{x}_t))$.
- 7: Perform gradient-guided conditional correction:
 $\mathbf{x}_{t-1} \leftarrow \mu_\theta(\mathbf{x}_t, t) - \sqrt{n}\sigma_t \cdot \frac{\nabla_{\mathbf{x}_t} \mathcal{L}(\mathbf{g}(\hat{\mathbf{x}}_0(\mathbf{x}_t)), \mathbf{g}_{\text{leaked}})}{\|\nabla_{\mathbf{x}_t} \mathcal{L}(\mathbf{g}(\hat{\mathbf{x}}_0(\mathbf{x}_t)), \mathbf{g}_{\text{leaked}})\|}$.
- 8: **end for**
- 9: **return** Reconstructed Image \mathbf{x}_0 .

In practice, deterministic sampling under a Gaussian spherical constraint minimizes the attack loss most rapidly.

However, noise-perturbed gradients make the corresponding target image non-smooth and deviate from the original target. To address this, we combine DDIM’s unconditional sampling direction with the optimal conditional sampling direction, thereby enhancing both generation quality and diversity. Specifically, line 7 in Algorithm 1 is refined as:

$$\begin{aligned} \mathbf{x}_{t-1} &= \mu_\theta(\mathbf{x}_t, t) + r \frac{d_m}{\|d_m\|}, \\ d_m &= d^{\text{sample}} + m_r(d^* - d^{\text{sample}}), \end{aligned} \quad (17)$$

where $d^* = -\sqrt{n}\sigma_t \cdot \frac{\nabla_{\mathbf{x}_t} \mathcal{L}(\mathbf{g}(\hat{\mathbf{x}}_0), \mathbf{g}^{\text{leaked}})}{\|\nabla_{\mathbf{x}_t} \mathcal{L}(\mathbf{g}(\hat{\mathbf{x}}_0), \mathbf{g}^{\text{leaked}})\|}$ represents the optimal adjustment direction derived from the leaked gradient $\mathbf{g}^{\text{leaked}}$, while $d^{\text{sample}} = \sigma_t \epsilon_t$ (with $\epsilon_t \sim \mathcal{N}(0, I)$) denotes DDIM’s stochastic unconditional sampling direction. Their weighted combination, d_m , is controlled by the guidance rate $m_r \in [0, 1]$, which balances these two objectives. The parameter r dictates the overall guidance step size.

This refined guidance mechanism strategically balances conditional guidance with sample quality, not only ensuring adherence to gradient-based conditions but also promoting smoother, higher-fidelity image generation. By leveraging DDIM’s inherent generative capability, we mitigate the adverse effects of noise-induced perturbations, potentially generating reconstructions closer to the original target.

5 Theoretical Analysis

This section establishes theoretical upper and lower bounds on the reconstruction error arising from posterior mean approximation, which is quantified by the Jensen gap in Section 4.2. Additionally, we analyze the convergence behavior of the attack loss. Furthermore, our analysis reveals the significant variation in GIA vulnerabilities across model architectures and proposes the RV metric to quantify a model’s intrinsic vulnerability to such attacks. Detailed proofs of Theorems are provided in Appendix A.

5.1 Bounds of Reconstruction Error

For Algorithm 1, Theorem 5.1 establishes the upper bound of the reconstruction error.

Theorem 5.1 (Upper Bound of Reconstruction Error). *Under the attacked model $F(\mathbf{x}; W)$, we assume that the adversary obtains a Gaussian noise-perturbed gradient $\mathbf{g}^{\text{leaked}} = \nabla_W F(\mathbf{x}_{\text{private}}; W) + \mathcal{N}(0, \sigma^2 I)$ corresponding to the private target $\mathbf{x}_{\text{private}}$. The gradient inversion attack is conducted according to Algorithm 1 under the approximation $p(\mathbf{g}^{\text{leaked}}|\mathbf{x}_t) \simeq p(\mathbf{g}^{\text{leaked}}|\hat{\mathbf{x}}_0(\mathbf{x}_t))$, where $\hat{\mathbf{x}}_0(\mathbf{x}_t)$ is the posterior mean of \mathbf{x}_0 given \mathbf{x}_t . Then, the reconstruction error—measured by the Jensen gap—is upper bounded by:*

$$\begin{aligned} \mathcal{J}(\mathbf{g}(\mathbf{x}), p(\mathbf{x}_0|\mathbf{x}_t)) &= |\mathbb{E}[\mathbf{g}(\mathbf{x}_0)] - \mathbf{g}(\mathbb{E}[\mathbf{x}_0])| \\ &\leq \frac{n}{\sqrt{2\pi}\sigma^2} \|\nabla_{\mathbf{x}} \mathbf{g}(\mathbf{x})\| \int \|\mathbf{x}_0 - \hat{\mathbf{x}}_0(\mathbf{x}_t)\| p(\mathbf{x}_0|\mathbf{x}_t) d\mathbf{x}_0, \end{aligned}$$

where n is \mathbf{x} ’s dimension, and $\mathbf{g}(\mathbf{x}) = \nabla_{\mathbf{x}} \nabla_W F(\mathbf{x}; W)$.

Jensen gap’s upper bound characterizes the worst-case reconstruction quality. The term $\int \|\mathbf{x}_0 - \hat{\mathbf{x}}_0(\mathbf{x}_t)\| p(\mathbf{x}_0|\mathbf{x}_t) d\mathbf{x}_0$, influenced by the pre-trained diffusion model (e.g., DDIM),

is sensitive to the noise scale σ^2 . Notably, our analysis identifies an architecture-dependent factor: $\|\nabla_{\mathbf{x}} \mathbf{g}(\mathbf{x})\| = \|\nabla_{\mathbf{x}} \nabla_W F(\mathbf{x}; W)\|$, which varies with input \mathbf{x} . We propose its upper bound, $\max_{\mathbf{x}} \|\nabla_{\mathbf{x}} \nabla_W F(\mathbf{x}; W)\|$, as a metric of F ’s vulnerability to GIAs. Using the Frobenius norm, we define this quantity as the model vulnerability measure.

Definition 5.1 (Reconstruction Vulnerability (RV)). *Let $F(\mathbf{x}; W)$ be a model parameterized by W , where \mathbf{x} denotes the input. The Reconstruction Vulnerability (RV) of F with respect to a private dataset \mathbb{X} is formally defined as:*

$$RV = \max_{\mathbf{x} \in \mathbb{X}} \|\nabla_{\mathbf{x}} \nabla_W F(\mathbf{x}; W)\|_F, \quad (18)$$

where $\|\cdot\|_F$ denotes the Frobenius norm.

A larger RV value signifies an increased sensitivity of parameter gradients to input variations, thus amplifying input-specific leakage and enabling higher-fidelity reconstruction. Since the direct calculation of RV is computationally intensive, we project $\nabla_W F(\mathbf{z}; W)$ onto M random orthogonal directions $\{\mathbf{v}_j\}_{j=1}^M$, where $\mathbf{v}_j \sim \mathbf{p}_{\mathbf{v}}$. For a model F trained on a dataset $\mathbb{X} = \{\mathbf{x}_i\}_{i=1}^{|\mathbb{X}|}$ with samples $\mathbf{x}_i \sim \mathbf{p}_{\text{data}}$, the RV value can be estimated as:

$$\begin{aligned} RV &= \mathbb{E}_{\mathbf{v} \sim \mathbf{p}_{\mathbf{v}}} \mathbb{E}_{\mathbf{x} \sim \mathbf{p}_{\text{data}}(\mathbf{x})} \|\nabla_{\mathbf{x}} (\mathbf{v}^T \nabla_W F(\mathbf{x}; W))\| \\ &\simeq \frac{1}{N} \frac{1}{M} \sum_{i=1}^N \sum_{j=1}^M \|\nabla_{\mathbf{x}} (\mathbf{v}_j^T \nabla_W F(\mathbf{x}_i; W))\| \end{aligned} \quad (19)$$

We then examine the lower bound of the reconstruction error. As shown in Equation (16), the properties of the attack loss function \mathcal{L} influence the lower bound of the Jensen gap. We rely on Assumptions 5.1-5.4 to derive the lower bound.

Assumption 5.1. \mathcal{L} is β -convex with respect to $\mathbf{g}(\mathbf{x})$;

Assumption 5.2. \mathcal{L} is α -smooth with respect to $\mathbf{g}(\mathbf{x})$;

Assumption 5.3. $\mathbf{g}(\mathbf{x})$ is L_g -smooth with respect to \mathbf{x} ;

Assumption 5.4. The Jacobian matrix $\mathbf{J}_{\mathbf{g}}(\mathbf{x}) = \nabla_{\mathbf{x}} \mathbf{g}(\mathbf{x})$ is full rank.

Theorem 5.2 (Lower Bound of Reconstruction Error). *Under the conditions of Theorem 5.1 and Assumptions 5.1-5.4, for $\mathbf{x} \in \mathbb{R}^n$, the Jensen Gap is lower bounded by:*

$$\begin{aligned} \mathcal{J}(\mathcal{L}(\mathbf{g}(\mathbf{x})), p(\mathbf{x}_0|\mathbf{x}_t)) &= |\mathbb{E}[\mathcal{L}(\mathbf{g}(\mathbf{x}_0))] - \mathcal{L}(\mathbf{g}(\mathbb{E}[\mathbf{x}_0]))| \\ &\geq \frac{1}{2} \left(\beta \lambda_{\min}(\mathbf{J}_{\mathbf{g}}(\mathbf{x})^T \mathbf{J}_{\mathbf{g}}(\mathbf{x})) - \alpha L_g \right) \sum_{i=1}^n \sigma_i^2, \end{aligned}$$

where $\lambda_{\min}(\cdot)$ represents the smallest eigenvalue of \cdot , L_g can be refined to a specific value $\frac{n}{\sqrt{2\pi}\sigma^2} \exp(-\frac{1}{2\sigma^2})$ under Gaussian-perturbed isotropic gradients, and $\{\sigma_i^2\}_{i=1}^n$ are the eigenvalues of the covariance matrix of $p(\mathbf{x}_0|\mathbf{x}_t)$.

In Theorem 5.2, $\lambda_{\min}(\mathbf{J}_{\mathbf{g}}(\mathbf{x})^T \mathbf{J}_{\mathbf{g}}(\mathbf{x}))$ can be interpreted as the information loss associated with the mapping $\mathbf{x} \mapsto \mathbf{g}$. This suggests that reconstructing an exact replica of the original private image from leaked gradients—even without explicit perturbation noise—is impossible. The degree of information loss is scaled by the randomness inherent in DDIM’s denoising steps, specifically by $\sum_{i=1}^n \sigma_i^2$. Moreover, Theorem 5.2 demonstrates that a larger noise scale σ^2 leads to a smaller value of L_g , which consequently increases the lower bound of the Jensen gap. In other words, the reconstruction error is positively correlated with the noise scale.

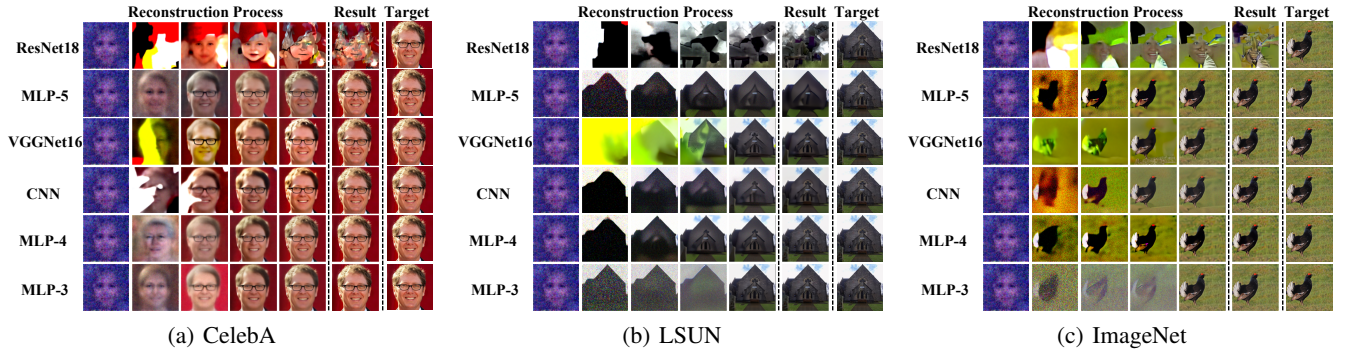


Figure 3: Reconstruction process of GSS-R. The *Reconstruction Process* columns display the intermediate reconstruction results $\hat{\mathbf{x}}_0(\mathbf{x}_t)$, while the *Result* and *Target* columns display the reconstructed results and target images, respectively.

5.2 Convergence of Attack Loss

A critical issue in GIA is whether the attack loss decreases as the reconstructed samples are progressively generated. Formally, we examine whether the sequence $\{\mathcal{L}(\mathbf{g}(\hat{\mathbf{x}}_0(\mathbf{x}_t)), \mathbf{g}^{\text{leaked}})\}_{t=T}^0$ decreases monotonically. If this holds, characterizing the decrease rate is essential. For simplicity, we denote $\mathcal{L}(\mathbf{x}_t) = \mathcal{L}(\mathbf{g}(\hat{\mathbf{x}}_0(\mathbf{x}_t)), \mathbf{g}^{\text{leaked}})$. Theorem 5.3 states the monotonic decrease of \mathcal{L} , and Theorem 5.4 provides a per-step lower bound on this decrease.

Theorem 5.3 (Convergence of Attack Loss). *Assume that the attack loss \mathcal{L} is α' -smooth and β' -strongly convex with respect to \mathbf{x} . When GIA is executed following Algorithm 1, the sequence $\{\mathcal{L}(\mathbf{x}_t)\}_{t=T}^0$ monotonically decreases as the denoising steps progress from timestep $t = T$ to $t = 0$.*

Theorem 5.4 (Convergence Rate of Attack Loss). *Under Assumptions 5.1-5.4, and assuming that the attack loss \mathcal{L} is α' -smooth and β' -strongly convex with respect to \mathbf{x} , if the attack loss is optimized using Algorithm 1, it satisfies:*

$$\mathcal{L}(\mathbf{x}_{t-1}) - \mathcal{L}(\mathbf{x}_t) \geq \frac{\beta' n \sigma_t^2}{2} + \beta' k \sqrt{n} \sigma_t + \frac{\beta' k^2}{2} - (k + \sqrt{n} \sigma_t) \left(\sqrt{\lambda_{\max}(\mathbf{J}_{\mathbf{g}}(\mathbf{x}) \mathbf{J}_{\mathbf{g}}(\mathbf{x})^T)} \cdot L_g \right),$$

where n is \mathbf{x} 's dimension, k is a positive constant, $\lambda_{\max}(\cdot)$ is the largest eigenvalue of \cdot , and $L_g = \frac{n}{\sqrt{2\pi}\sigma^2} \exp(-\frac{1}{2\sigma^2})$.

As discussed in Theorem 5.2, the private information loss associated with the mapping $\mathbf{x} \mapsto \mathbf{g}$ is quantified by the term $\sqrt{\lambda_{\max}(\mathbf{J}_{\mathbf{g}}(\mathbf{x}) \mathbf{J}_{\mathbf{g}}(\mathbf{x})^T)}$. The rate of attack loss reduction is further influenced by L_g , where $L_g \leq \frac{n}{\sqrt{2\pi}\sigma^2}$. Consequently, a larger noise scale σ^2 results in a smaller lower bound for $\mathcal{L}(\mathbf{x}_{t-1}) - \mathcal{L}(\mathbf{x}_t)$, which, in turn, degrades the reconstruction performance.

6 Experiments

6.1 Experimental Setup

Datasets and Models. Experiments were conducted on three datasets: CelebA (Karras et al. 2017a), LSUN (Yu et al. 2015), and ImageNet (Deng et al. 2009), with images of 256×256 resolution. The attacked models include MLPs

with 3/4/5 layers (MLP-3/4/5), CNN, ResNet18 (He et al. 2016), and VGGNet16 (Simonyan and Zisserman 2014). The pre-trained diffusion model, consistently sourced from (Chung et al. 2022a), was trained on the FFHQ dataset (Karras et al. 2017b), processing 256×256 resolution images.

Hyperparameters. We employ conditional reverse sampling in Equation (17), a common practice. We set a gradient acquisition batch size of 1 and a guidance rate m_r of 0.20. The attack loss is measured using the Euclidean distance. All RV values are computed with $M = 1000$ and $N = 310$.

Evaluation Metrics. Reconstruction quality is evaluated using three widely adopted computer vision metrics: MSE, PSNR, and LPIPS, which quantify the similarity between the reconstructions and the original target images.

Baselines. We compared our GSS-R with baseline approaches, including DLG (Zhu, Liu, and Han 2019), IG (Geiping et al. 2020b), GI (Yin et al. 2021b), GIAS (Jeon et al. 2021a), GGL (Li et al. 2022b), GIFD (Fang et al. 2023a), and FinetunedDiff (Meng et al. 2024).

Additional detailed settings are provided in Appendix B.

6.2 Experimental Results

GIA with Original Gradients and RV Metric Validation. This section presents reconstruction results obtained with original, unperturbed gradients. For each attacked model, we first compute its RV value and then perform our GSS-R attack. Figure 3 visually illustrates the reconstruction results, with attacked models ordered by increasing RV values. Table 1 further quantifies the reconstruction performance.

Based on these results, we highlight two key findings: (i) Robustness across diverse distributions. Despite diffusion models being pre-trained on the FFHQ face dataset, GSS-R effectively reconstructs high-fidelity images across diverse distributions. This demonstrates our attack's robustness and generalization, enabling efficient GIAs without requiring prior knowledge of the target data distribution—a common limitation in existing generative model-based approaches; (ii) RV as an effective vulnerability indicator. Models with higher RV values consistently exhibit higher reconstruction

Dataset	Model	RV	MSE↓	PSNR↑	LPIPS↓
CelebA	ResNet18	0.17	9.46e-2	10.79	4.14e-4
	MLP-5	8.71	3.13e-5	45.05	9.84e-8
	VGGNet16	10.74	1.26e-4	40.76	2.43e-7
	CNN	18.51	7.72e-5	41.12	2.05e-7
	MLP-4	20.85	3.08e-5	45.12	8.92e-8
	MLP-3	52.73	4.55e-5	43.42	1.60e-7
LSUN	ResNet18	0.17	1.00e-1	9.99	3.10e-4
	MLP-5	8.71	2.27e-3	26.44	3.09e-5
	VGGNet16	10.74	6.63e-3	22.79	4.88e-5
	CNN	18.51	2.54e-3	25.95	2.44e-5
	MLP-4	20.85	3.61e-4	34.43	5.60e-7
	MLP-3	52.73	1.48e-4	38.29	4.03e-7
ImageNet	ResNet18	0.17	4.45e-2	13.52	2.54e-4
	MLP-5	8.71	3.34e-4	25.35	3.58e-5
	VGGNet16	10.74	1.07e-3	29.71	1.48e-6
	CNN	18.51	1.15e-4	27.39	2.55e-5
	MLP-4	20.85	3.09e-4	25.10	4.05e-5
	MLP-3	52.73	1.05e-4	28.00	1.63e-5

Table 1: Quantitative analysis of the reconstruction quality across various datasets and attacked models.

quality, indicating a higher risk of privacy leakage. Specifically, we observe that the reconstruction performance increases convexly with RV. This finding suggests designing models with lower RV values due to their inherent lower gradient privacy risk. Furthermore, architectural modifications to low-RV models warrant particular caution, as even minor increases in RV can significantly increase privacy risks.

Reconstruction with Noise-Perturbed Gradients. When the leaked gradient is perturbed by Gaussian noise, the target image corresponding to $\mathbf{g}_{\text{leaked}}$ deviates from the original target. We define this distorted target as $\mathbf{x}_{\text{noisy}}$. This section investigates the effectiveness of added noise in impeding our attack and validates our theoretical findings.

Figure 4 illustrates the reconstruction process on CelebA under varying Gaussian noise magnitudes σ^2 added to CNN gradients. It reveals that the PSNR between the intermediate reconstructions $\hat{\mathbf{x}}_0(\mathbf{x}_t)$ and the original target image $\mathbf{x}_{\text{private}}$ exhibits a non-monotonic behavior, peaking before subsequently declining. This phenomenon is attributed to the inherent denoising capability of diffusion models. Rather than directly converging from a randomly initialized dummy image to the distorted target $\mathbf{x}_{\text{noisy}}$, the reconstruction process produces smoother intermediate results that more closely approximate $\mathbf{x}_{\text{private}}$. However, as reconstruction iterations progress, the model’s denoising capacity becomes insufficient to counteract the noise inherent in $\mathbf{x}_{\text{noisy}}$. Consequently, the reconstruction begins to converge toward $\mathbf{x}_{\text{noisy}}$ and deviates from $\mathbf{x}_{\text{private}}$, explaining the observed decline in performance during the later stages. The quantitative results in Table 2 corroborate these observations.

Experimental results also validate our theoretical findings: (i) Effect of noise scale on reconstruction error. The reconstruction quality degrades noticeably as the noise magnitude increases. This observation aligns with our theoretical analysis (Theorems 5.1-5.2), which establishes that larger noise levels amplify the Jensen gap, leading to more chal-

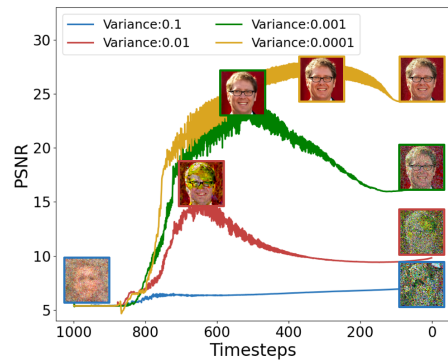


Figure 4: Reconstruction processes on CelebA with noise-perturbed CNN gradients. Reconstructed images at peak performance and at the end of reconstruction are displayed.

Gaussian Variance	MSE↓	PSNR↑	LPIPS↓
10^{-4}	0.0016	28.0343	7.9935e-6
10^{-3}	0.0039	24.0567	4.5263e-5
10^{-2}	0.0366	14.9784	2.4762e-4
10^{-1}	0.1252	9.0236	7.1237e-4

Table 2: Quantitative analysis on reconstruction quality on CelebA with Gaussian noise-perturbed CNN gradients. Metrics are reported between the intermediate reconstructions $\hat{\mathbf{x}}_0(\mathbf{x}_t)$ at peak performance and the original target $\mathbf{x}_{\text{private}}$.

lenging accurate reconstruction; (ii) Attack loss reduction during gradient-guided reverse sampling. According to Theorem 5.3, the attack loss in Algorithm 1 decreases monotonically as the process evolves from random noise towards the original target $\mathbf{x}_{\text{private}}$, achieving optimal reconstruction at convergence. In our implementation, we modified line 7 of Algorithm 1 by incorporating the mechanism in Equation (17), leveraging DDIM’s generative prior to enhance reconstruction smoothness and quality. This adjustment yields earlier peaks in PSNR, though reconstruction quality eventually declines due to gradient perturbations introduced by noise; (iii) Attack loss reduction rate. Theorem 5.4 states that the rate of attack loss reduction depends on the noise scale: larger noise levels result in smaller $\mathcal{L}(\mathbf{x}_{t-1}) - \mathcal{L}(\mathbf{x}_t)$, indicating slower improvements in reconstruction quality and lower final reconstruction quality. This trend is empirically confirmed in Figure 4, where higher noise variance leads to a slower PSNR increase and reduced reconstruction fidelity.

Comparison with Baselines. To demonstrate the superior performance of our GSS-R, we conducted a comprehensive comparison with state-of-the-art baselines on CelebA, using CNN as the attacked model. Table 3 reports the quantitative results of GIAs with original gradients. As shown in Table 3, our approach successfully guides the diffusion model to reconstruct high-resolution images with markedly improved fidelity, underscoring the heightened privacy risks when adversaries gain access to unprotected gradients.

We also extended the comparison to evaluate reconstruction performance using CNN gradients perturbed by Gaus-

Method	MSE↓	PSNR↑	LPIPS↓
DLG (Zhu, Liu, and Han 2019)	0.0480	13.1835	2.3453e-4
IG (Geiping et al. 2020b)	0.0196	17.0756	1.1612e-4
GI (Yin et al. 2021b)	0.0223	16.5109	1.4274e-4
GIAS (Jeon et al. 2021a)	0.0458	13.3885	3.9351e-4
GGL (Li et al. 2022b)	0.0179	17.4923	1.1937e-4
GIFD (Fang et al. 2023a)	0.0098	20.0534	6.6672e-5
FinetunedDiff (Meng et al. 2024)	0.0011	29.4490	5.4441e-6
GSS-R (Ours)	0.0001	41.1229	2.0519e-7

Table 3: Quantitative analysis of baselines and our GSS-R with original, unperturbed gradients.

sian noise ($\sigma^2 = 0.01$). As detailed in Table 4, our methods demonstrate improved robustness against noise-perturbed gradients. Specifically, GSS-R achieves the highest PSNR, surpassing the optimal baseline, GGL, by 1.0802 dB. These results underscore that simple noise addition is insufficient to ensure gradient privacy, highlighting the need for more sophisticated mitigation strategies in practical applications.

Method	MSE↓	PSNR↑	LPIPS↓
DLG (Zhu, Liu, and Han 2019)	0.2194	6.5871	1.8540e-3
IG (Geiping et al. 2020b)	0.0747	11.2677	3.2103e-4
GI (Yin et al. 2021b)	0.0892	10.4968	5.6760e-4
GIAS (Jeon et al. 2021a)	0.0613	12.1276	3.4494e-4
GGL (Li et al. 2022b)	0.0394	13.8982	2.5247e-4
GIFD (Fang et al. 2023a)	0.0425	13.7118	2.5901e-4
FinetunedDiff (Meng et al. 2024)	0.0683	11.6675	3.0877e-4
GSS-R (Ours)	0.0366	14.9784	2.4762e-4

Table 4: Quantitative analysis of baselines and our method with Gaussian noise ($\sigma^2 = 0.01$)-perturbed gradients.

6.3 Ablation Studies

Impact of Batch Size. We analyze the impact of gradient acquisition batch size B on the reconstruction performance using the CelebA dataset. As illustrated in Table 5, reconstruction quality consistently decreases with increasing batch size across all attack methods. This degradation arises from the averaging effect of batching, which blurs individual image-specific gradient information and thereby reduces reconstruction fidelity. However, GSS-R consistently outperforms all baselines across all batch sizes, owing to the strong generative capability of diffusion models combined with pixel-level conditional guidance.

Impact of Guidance Rate. Table 6 presents the effect of varying the guidance rate m_r on reconstruction quality. The guidance rate, which we explored within the range of 0.01 to 0.80, controls the trade-off between conditional guidance and sample diversity. Optimal reconstruction metrics are observed at $m_r = 0.20$, yielding the lowest MSE ($7.7215e-5$), highest PSNR (41.1230), and lowest LPIPS ($2.0519e-7$).

Impact of Noise Type. To evaluate the impact of noise types on reconstruction performance in noise-based defenses, we conducted experiments by perturbing gradients with varying magnitudes of Laplacian noise. Table 7 quantitatively evaluates the reconstruction performance at peak

Method	$B = 1$	$B = 2$	$B = 4$	$B = 8$
DLG (Zhu, Liu, and Han 2019)	13.1835	11.0356	9.9452	8.3562
IG (Geiping et al. 2020b)	17.0756	15.2562	11.3003	9.5382
GI (Yin et al. 2021b)	16.5109	14.8351	11.0352	9.2350
GIAS (Jeon et al. 2021a)	13.3885	11.4684	10.2465	8.9462
GGL (Li et al. 2022b)	17.4923	15.5526	-	-
GIFD (Fang et al. 2023a)	20.0534	18.3562	13.9636	10.3425
FinetunedDiff (Meng et al. 2024)	29.4490	21.4583	15.6387	11.4570
GSS-R (Ours)	41.1229	24.4602	17.4791	12.1425

Table 5: Impact of batch size for gradient acquisition on PSNR of reconstruction results. Note that StyleGAN2’s latent vector involves a large number of parameters for optimization and the CMA-ES optimizer, adopted by GGL, does not support large-scale optimization. GGL is consequently restricted to operating with batch sizes $B > 2$.

Guidance Rate	MSE↓	PSNR↑	LPIPS↓
0.01	2.0406e-3	26.9023	6.9703e-6
0.10	2.1778e-4	36.6198	4.1730e-7
0.20	7.7215e-5	41.1229	2.0519e-7
0.30	1.4769e-4	38.3065	2.8713e-7
0.40	1.0778e-4	39.6746	1.9574e-7
0.60	2.0407e-4	36.9023	9.0661e-7
0.80	2.7478e-4	35.6101	1.1251e-6

Table 6: Impact of guidance rate on reconstruction quality.

performance. Comparing these results with attacks on Gaussian noise-perturbed gradients (Table 2), we find that the reconstruction quality is primarily determined by the noise magnitude. The specific type of noise exhibits a negligible influence on reconstruction performance.

Laplacian Variance	MSE↓	PSNR↑	LPIPS↓
10^{-4}	0.0016	27.9395	9.3180e-6
10^{-3}	0.0038	24.2073	3.7156e-5
10^{-2}	0.0304	15.1657	2.3746e-4
10^{-1}	0.1390	8.5697	5.6100e-4

Table 7: Quantitative analysis on reconstruction quality with Laplacian noise-perturbed CNN gradients.

More details of running time and GPU usage are provided in Appendix C.

7 Conclusion and Future Work

In this paper, we propose a novel GIA method based on conditional diffusion models to recover higher-quality images from noise-perturbed gradients. Our approach requires minimal modifications to the standard reverse diffusion process and does not rely on prior knowledge. Leveraging generative capability of diffusion models, our attack effectively mitigates the impact of noise perturbation. We also provide theoretical bounds on the reconstruction error and prove the convergence of the attack loss. Our analysis reveals the intrinsic vulnerability of diverse model architectures to GIAs. Extensive experiments validate the effectiveness of our attack and demonstrate its superiority in recovering high-quality reconstructions from noise-perturbed gradients.

Acknowledgments

This study was funded by The Natural Science Foundation of Fujian Province (Grant numbers [2024J08276,2024J08278]), The Key Research Project for Young and Middle-aged Researchers by the Fujian Provincial Department of Education (Grant numbers [JZ230044]).

References

- Chung, H.; Kim, J.; Mccann, M. T.; Klasky, M. L.; and Ye, J. C. 2022a. Diffusion posterior sampling for general noisy inverse problems. *arXiv preprint arXiv:2209.14687*.
- Chung, H.; Kim, J.; Mccann, M. T.; Klasky, M. L.; and Ye, J. C. 2022b. Diffusion posterior sampling for general noisy inverse problems. *arXiv preprint arXiv:2209.14687*.
- Chung, H.; Sim, B.; Ryu, D.; and Ye, J. C. 2022c. Improving diffusion models for inverse problems using manifold constraints. *Advances in Neural Information Processing Systems*, 35: 25683–25696.
- Deng, J.; Dong, W.; Socher, R.; Li, L.-J.; Li, K.; and Fei-Fei, L. 2009. Imagenet: A large-scale hierarchical image database. In *2009 IEEE conference on computer vision and pattern recognition*, 248–255. Ieee.
- Dhariwal, P.; and Nichol, A. 2021. Diffusion models beat gans on image synthesis. *Advances in neural information processing systems*, 34: 8780–8794.
- El Mestari, S. Z.; Lenzini, G.; and Demirci, H. 2024. Preserving data privacy in machine learning systems. *Computers & Security*, 137: 103605.
- Fang, H.; Chen, B.; Wang, X.; Wang, Z.; and Xia, S.-T. 2023a. GIFD: A Generative Gradient Inversion Method with Feature Domain Optimization. In *Proceedings of the IEEE/CVF International Conference on Computer Vision*, 4967–4976.
- Fang, H.; Chen, B.; Wang, X.; Wang, Z.; and Xia, S.-T. 2023b. GIFD: A Generative Gradient Inversion Method with Feature Domain Optimization. In *Proceedings of the IEEE/CVF International Conference on Computer Vision*, 4967–4976.
- Geiping, J.; Bauermeister, H.; Dröge, H.; and Moeller, M. 2020a. Inverting gradients-how easy is it to break privacy in federated learning? *Advances in Neural Information Processing Systems*, 33: 16937–16947.
- Geiping, J.; Bauermeister, H.; Dröge, H.; and Moeller, M. 2020b. Inverting gradients-how easy is it to break privacy in federated learning? *Advances in Neural Information Processing Systems*, 33: 16937–16947.
- He, K.; Zhang, X.; Ren, S.; and Sun, J. 2016. Deep residual learning for image recognition. In *Proceedings of the IEEE conference on computer vision and pattern recognition*, 770–778.
- He, Y.; Murata, N.; Lai, C.-H.; Takida, Y.; Uesaka, T.; Kim, D.; Liao, W.-H.; Mitsufuji, Y.; Kolter, J. Z.; Salakhutdinov, R.; et al. 2023. Manifold preserving guided diffusion. *arXiv preprint arXiv:2311.16424*.
- Ho, J.; Jain, A.; and Abbeel, P. 2020a. Denoising diffusion probabilistic models. *Advances in neural information processing systems*, 33: 6840–6851.
- Ho, J.; Jain, A.; and Abbeel, P. 2020b. Denoising diffusion probabilistic models. *Advances in neural information processing systems*, 33: 6840–6851.
- Ho, J.; and Salimans, T. 2022. Classifier-free diffusion guidance. *arXiv preprint arXiv:2207.12598*.
- Jeon, J.; Lee, K.; Oh, S.; Ok, J.; et al. 2021a. Gradient inversion with generative image prior. *Advances in neural information processing systems*, 34: 29898–29908.
- Jeon, J.; Lee, K.; Oh, S.; Ok, J.; et al. 2021b. Gradient inversion with generative image prior. *Advances in neural information processing systems*, 34: 29898–29908.
- Kairouz, P.; McMahan, H. B.; Avent, B.; Bellet, A.; Bennis, M.; Bhagoji, A. N.; Bonawitz, K.; Charles, Z.; Cormode, G.; Cummings, R.; et al. 2021. Advances and open problems in federated learning. *Foundations and trends® in machine learning*, 14(1–2): 1–210.
- Karras, T.; Aila, T.; Laine, S.; and Lehtinen, J. 2017a. Progressive growing of gans for improved quality, stability, and variation. *arXiv preprint arXiv:1710.10196*.
- Karras, T.; Aila, T.; Laine, S.; and Lehtinen, J. 2017b. Progressive growing of gans for improved quality, stability, and variation. *arXiv preprint arXiv:1710.10196*.
- Laurent, B.; and Massart, P. 2000. Adaptive estimation of a quadratic functional by model selection. *Annals of statistics*, 1302–1338.
- Ledoux, M. 2001. *The concentration of measure phenomenon*. 89. American Mathematical Soc.
- Li, T.; Sahu, A. K.; Talwalkar, A.; and Smith, V. 2020. Federated learning: Challenges, methods, and future directions. *IEEE signal processing magazine*, 37(3): 50–60.
- Li, Z.; Zhang, J.; Liu, L.; and Liu, J. 2022a. Auditing privacy defenses in federated learning via generative gradient leakage. In *Proceedings of the IEEE/CVF Conference on Computer Vision and Pattern Recognition*, 10132–10142.
- Li, Z.; Zhang, J.; Liu, L.; and Liu, J. 2022b. Auditing privacy defenses in federated learning via generative gradient leakage. In *Proceedings of the IEEE/CVF Conference on Computer Vision and Pattern Recognition*, 10132–10142.
- Meng, J.; Huang, T.; Chen, H.; and Li, C. 2024. Is Diffusion Model Safe? Severe Data Leakage via Gradient-Guided Diffusion Model. *arXiv preprint arXiv:2406.09484*.
- Nichol, A. Q.; and Dhariwal, P. 2021. Improved denoising diffusion probabilistic models. In *International Conference on Machine Learning*, 8162–8171. PMLR.
- Rombach, R.; Blattmann, A.; Lorenz, D.; Esser, P.; and Ommer, B. 2022. High-resolution image synthesis with latent diffusion models. In *Proceedings of the IEEE/CVF conference on computer vision and pattern recognition*, 10684–10695.
- Simonyan, K.; and Zisserman, A. 2014. Very deep convolutional networks for large-scale image recognition. *arXiv preprint arXiv:1409.1556*.

Song, J.; Meng, C.; and Ermon, S. 2020. Denoising diffusion implicit models. *arXiv preprint arXiv:2010.02502*.

Song, Y.; and Ermon, S. 2019. Generative modeling by estimating gradients of the data distribution. *Advances in neural information processing systems*, 32.

Song, Y.; Sohl-Dickstein, J.; Kingma, D. P.; Kumar, A.; Ermon, S.; and Poole, B. 2020. Score-based generative modeling through stochastic differential equations. *arXiv preprint arXiv:2011.13456*.

Wang, J.; Guo, S.; Xie, X.; and Qi, H. 2022. Protect privacy from gradient leakage attack in federated learning. In *IEEE INFOCOM 2022-IEEE Conference on Computer Communications*, 580–589. IEEE.

Yang, L.; Ding, S.; Cai, Y.; Yu, J.; Wang, J.; and Shi, Y. 2024. Guidance with spherical gaussian constraint for conditional diffusion. *arXiv preprint arXiv:2402.03201*.

Yin, H.; Mallya, A.; Vahdat, A.; Alvarez, J. M.; Kautz, J.; and Molchanov, P. 2021a. See through gradients: Image batch recovery via gradinversion. In *Proceedings of the IEEE/CVF Conference on Computer Vision and Pattern Recognition*, 16337–16346.

Yin, H.; Mallya, A.; Vahdat, A.; Alvarez, J. M.; Kautz, J.; and Molchanov, P. 2021b. See through gradients: Image batch recovery via gradinversion. In *Proceedings of the IEEE/CVF Conference on Computer Vision and Pattern Recognition*, 16337–16346.

Yu, F.; Seff, A.; Zhang, Y.; Song, S.; Funkhouser, T.; and Xiao, J. 2015. Lsun: Construction of a large-scale image dataset using deep learning with humans in the loop. *arXiv preprint arXiv:1506.03365*.

Yu, J.; Wang, Y.; Zhao, C.; Ghanem, B.; and Zhang, J. 2023. Freedom: Training-free energy-guided conditional diffusion model. In *Proceedings of the IEEE/CVF International Conference on Computer Vision*, 23174–23184.

Zhao, B.; Mopuri, K. R.; and Bilen, H. 2020. idlg: Improved deep leakage from gradients. *arXiv preprint arXiv:2001.02610*.

Zhu, L.; Liu, Z.; and Han, S. 2019. Deep leakage from gradients. *Advances in neural information processing systems*, 32.

A Proofs of Theorems

A.1 Proof of Theorem 5.1

Theorem 5.1 (Upper Bound of Reconstruction Error). Under the attacked model $F(\mathbf{x}; W)$, we assume that the adversary obtains a Gaussian noise-perturbed gradient $\mathbf{g}_{\text{leaked}} = \nabla_W F(\mathbf{x}_{\text{private}}; W) + \mathcal{N}(0, \sigma^2 I)$ corresponding to the private target $\mathbf{x}_{\text{private}}$. The gradient inversion attack is conducted according to Algorithm 1 under the approximation $p(\mathbf{g}_{\text{leaked}}|\mathbf{x}_t) \simeq p(\mathbf{g}_{\text{leaked}}|\hat{\mathbf{x}}_0(\mathbf{x}_t))$, where $\hat{\mathbf{x}}_0(\mathbf{x}_t)$ is the posterior mean of \mathbf{x}_0 given \mathbf{x}_t . Then, the reconstruction error—measured by the Jensen gap—is upper bounded by:

$$\begin{aligned} \mathcal{J}(\mathbf{g}(\mathbf{x}), p(\mathbf{x}_0|\mathbf{x}_t)) &= |\mathbb{E}[\mathbf{g}(\mathbf{x}_0)] - \mathbf{g}(\mathbb{E}[\mathbf{x}_0])| \\ &\leq \frac{n}{\sqrt{2\pi\sigma^2}} \|\nabla_{\mathbf{x}} \mathbf{g}(\mathbf{x})\| \int \|\mathbf{x}_0 - \hat{\mathbf{x}}_0(\mathbf{x}_t)\| p(\mathbf{x}_0|\mathbf{x}_t) d\mathbf{x}_0, \end{aligned}$$

where n is \mathbf{x} 's dimension, and $\mathbf{g}(\mathbf{x}) = \nabla_{\mathbf{x}} \nabla_W F(\mathbf{x}; W)$.

Proof of Theorem 5.1. Analogous to the proof of Theorem 1 in (Chung et al. 2022b), the upper bound of the Jensen Gap is:

$$\begin{aligned} \mathcal{J}(\mathbf{g}(\mathbf{x}), p(\mathbf{x}_0|\mathbf{x}_t)) &\leq \frac{n}{\sqrt{2\pi\sigma^2}} \exp\left(-\frac{1}{2\sigma^2}\right) \|\nabla_{\mathbf{x}} \mathbf{g}(\mathbf{x})\| \int \|\mathbf{x}_0 - \hat{\mathbf{x}}_0(\mathbf{x}_t)\| p(\mathbf{x}_0|\mathbf{x}_t) d\mathbf{x}_0 \\ &\leq \frac{n}{\sqrt{2\pi\sigma^2}} \|\nabla_{\mathbf{x}} \mathbf{g}(\mathbf{x})\| \int \|\mathbf{x}_0 - \hat{\mathbf{x}}_0(\mathbf{x}_t)\| p(\mathbf{x}_0|\mathbf{x}_t) d\mathbf{x}_0. \end{aligned} \tag{20}$$

The final inequality holds because $\frac{\exp(-\frac{1}{2\sigma^2})}{\sigma^2} \leq \frac{1}{\sigma^2}$. □

A.2 Proof of Theorem 5.2

Theorem 5.2 (Lower Bound of Reconstruction Error). Under the conditions of Theorem 5.1 and Assumptions 5.1-5.4, for $\mathbf{x} \in \mathbb{R}^n$, the Jensen Gap is lower bounded by:

$$\begin{aligned} \mathcal{J}(\mathcal{L}(\mathbf{g}(\mathbf{x})), \mathbf{g}_{\text{leaked}}, p(\mathbf{x}_0|\mathbf{x}_t)) &= |\mathbb{E}[\mathcal{L}(\mathbf{g}(\mathbf{x}_0))] - \mathcal{L}(\mathbf{g}(\mathbb{E}[\mathbf{x}_0]))| \\ &\geq \frac{1}{2} (\beta \lambda_{\min}(\mathbf{J}_{\mathbf{g}}(\mathbf{x})^T \mathbf{J}_{\mathbf{g}}(\mathbf{x})) - \alpha L_g) \sum_{i=1}^n \sigma_i^2, \end{aligned}$$

where $\lambda_{\min}(\cdot)$ represents the smallest eigenvalue of \cdot , L_g can be refined to a specific value $\frac{n}{\sqrt{2\pi\sigma^2}} \exp(-\frac{1}{2\sigma^2})$ under Gaussian-perturbed isotropic gradients, and $\{\sigma_i^2\}_{i=1}^n$ are the eigenvalues of the covariance matrix of $p(\mathbf{x}_0|\mathbf{x}_t)$.

To prove Theorem 5.2, we introduce Lemma A.1 and Lemma A.2.

Lemma A.1 ((Chung et al. 2022b)). *Under the conditions of Theorem 5.1, if the attack loss \mathcal{L} is β' -strongly convex with respect to \mathbf{x} and $p(\mathbf{x}_0|\mathbf{x}_t)$ is a Gaussian distribution with covariance matrix whose eigenvalues are $\{\sigma_i^2\}_{i=1}^n$. Then the lower bound of Jensen Gap is bounded by:*

$$\mathcal{J}(\mathcal{L}(\mathbf{g}(\mathbf{x})), \mathbf{g}_{\text{leaked}}, p(\mathbf{x}_0|\mathbf{x}_t)) \geq \frac{1}{2} \beta' \sum_{i=1}^n \sigma_i^2. \tag{21}$$

Lemma A.2 ((Chung et al. 2022b)). *Let $\phi(\cdot)$ be an isotropic multivariate Gaussian density function with variance matrix $\sigma^2 I$. There exists a constant L such that $\forall \mathbf{x}, \mathbf{y} \in \mathbb{R}^n$,*

$$\|\phi(\mathbf{x}) - \phi(\mathbf{y})\| \leq L \|\mathbf{x} - \mathbf{y}\|, \tag{22}$$

where $L = \frac{n}{\sqrt{2\pi\sigma^2}} \exp(-\frac{1}{2\sigma^2})$.

We omit the proofs of Lemmas A.1 and A.2 as they are provided in (Chung et al. 2022b).

Proof of Theorem 5.2. For simplicity, we denote $\mathcal{L}(\mathbf{g}(\mathbf{x}), \mathbf{g}_{\text{leaked}})$ as $\mathcal{L}(\mathbf{g}(\mathbf{x}))$ within the proof. Taking Taylor's expansion of $\mathcal{L}(\mathbf{g}(\mathbf{x}))$ around $\mathbf{g}(\mathbf{y})$, we get:

$$\mathcal{L}(\mathbf{g}(\mathbf{x})) = \mathcal{L}(\mathbf{g}(\mathbf{y})) + (\mathbf{J}_{\mathbf{g}}(\mathbf{x})^T \nabla_{\mathbf{g}} \mathcal{L}(\mathbf{g}(\mathbf{x})))^T (\mathbf{x} - \mathbf{y}) + \frac{1}{2} (\mathbf{x} - \mathbf{y})^T \nabla^2 \mathcal{L}(\mathbf{g}(\mathbf{c})) (\mathbf{x} - \mathbf{y}), \tag{23}$$

where $\nabla^2 \mathcal{L}(\mathbf{g}(\mathbf{x}))$ denotes the Hessian matrix of \mathcal{L} with respect to \mathbf{x} , $\mathbf{J}_{\mathbf{g}}(\mathbf{x}) = \nabla_{\mathbf{x}} \mathbf{g}(\mathbf{x})$ is the Jacobian of $\mathbf{g}(\mathbf{x})$, and \mathbf{c} is a point such that $\mathbf{g}(\mathbf{c}) \in [\mathbf{g}(\mathbf{x}), \mathbf{g}(\mathbf{y})]$.

Next, we analyze the Hessian matrix $\nabla^2 \mathcal{L}(\mathbf{g}(\mathbf{x}))$:

$$\nabla^2 \mathcal{L}(\mathbf{g}(\mathbf{x})) = \nabla_{\mathbf{x}} (\mathbf{J}_{\mathbf{g}}(\mathbf{x})^T \nabla_{\mathbf{g}} \mathcal{L}(\mathbf{g}(\mathbf{x}))) = \mathbf{J}_{\mathbf{g}}(\mathbf{x})^T \nabla_{\mathbf{g}}^2 \mathcal{L}(\mathbf{g}(\mathbf{x})) \mathbf{J}_{\mathbf{g}}(\mathbf{x}) + \sum_{i=1}^m \nabla \mathcal{L}_i(\mathbf{g}(\mathbf{x})) \nabla_{\mathbf{x}}^2 \mathbf{g}_i(\mathbf{x}), \quad (24)$$

where $\nabla \mathcal{L}_i(\mathbf{g}(\mathbf{x})) = \frac{\partial \mathcal{L}}{\partial \mathbf{g}_i(\mathbf{x})}$ and m is the dimension of $\mathbf{g}(\mathbf{x})$. $\nabla^2 \mathbf{g}_i(\mathbf{x})$ is the Hessian matrix of the i -th component of $\mathbf{g}(\mathbf{x})$ with respect to \mathbf{x} . Since \mathcal{L} is β -convex with respect to $\mathbf{g}(\mathbf{x})$, we have $\beta I \preceq \nabla_{\mathbf{g}}^2 \mathcal{L}(\mathbf{g}(\mathbf{x}))$. This implies:

$$\beta \lambda_{\min} (\mathbf{J}_{\mathbf{g}}(\mathbf{x})^T \mathbf{J}_{\mathbf{g}}(\mathbf{x})) I \preceq \beta \mathbf{J}_{\mathbf{g}}(\mathbf{x})^T \mathbf{J}_{\mathbf{g}}(\mathbf{x}) \preceq \mathbf{J}_{\mathbf{g}}(\mathbf{x})^T \nabla_{\mathbf{g}}^2 \mathcal{L}(\mathbf{g}(\mathbf{x})) \mathbf{J}_{\mathbf{g}}(\mathbf{x}), \quad (25)$$

where $\lambda_{\min}(\cdot)$ represents the smallest eigenvalue of a matrix.

Furthermore, given that $\mathbf{g}(\mathbf{x})$ is L_g -smooth with respect to \mathbf{x} , we have $\|\nabla^2 \mathbf{g}_i(\mathbf{x})\| \leq L_g$. And since \mathcal{L} is α -smooth with respect to $\mathbf{g}(\mathbf{x})$, it follows that $\|\nabla \mathcal{L}_i(\mathbf{g}(\mathbf{x}))\| \leq \alpha$. Therefore, for the summation term:

$$\left\| \sum_{i=1}^m \nabla \mathcal{L}_i(\mathbf{g}(\mathbf{x})) \nabla_{\mathbf{x}}^2 \mathbf{g}_i(\mathbf{x}) \right\| \leq m \alpha L_g. \quad (26)$$

Combining these results, we establish a lower bound for $\nabla^2 \mathcal{L}(\mathbf{g}(\mathbf{x}))$:

$$\beta \lambda_{\min} (\mathbf{J}_{\mathbf{g}}(\mathbf{x})^T \mathbf{J}_{\mathbf{g}}(\mathbf{x})) I - m \alpha L_g I \preceq \nabla^2 \mathcal{L}(\mathbf{g}(\mathbf{x})) \quad (27)$$

The supremum of the smallest eigenvalue of $\nabla^2 \mathcal{L}(\mathbf{g}(\mathbf{c}))$ is therefore:

$$\sup(\lambda_{\min}(\nabla^2 \mathcal{L}(\mathbf{g}(\mathbf{c})))) = \beta \lambda_{\min} (\mathbf{J}_{\mathbf{g}}(\mathbf{x})^T \mathbf{J}_{\mathbf{g}}(\mathbf{x})) - \alpha L_g. \quad (28)$$

Consequently, $\mathcal{L}(\mathbf{g}(\mathbf{x}))$ is β' -convex, where $\beta' = \beta \lambda_{\min} (\mathbf{J}_{\mathbf{g}}(\mathbf{x})^T \mathbf{J}_{\mathbf{g}}(\mathbf{x})) - \alpha L_g$. According to Lemma A.1, the lower bound of the Jensen Gap is bounded by $\frac{1}{2} \beta' \sum_{i=1}^n \sigma_i^2$:

$$\mathcal{J}(\mathcal{L}(\mathbf{g}(\mathbf{x})), p(\mathbf{x}_0|\mathbf{x}_t)) = \mathcal{J}(\mathcal{L}(\mathbf{g}(\mathbf{x}), \mathbf{g}_{\text{leaked}}), p(\mathbf{x}_0|\mathbf{x}_t)) \geq \frac{1}{2} (\beta \lambda_{\min} (\mathbf{J}_{\mathbf{g}}(\mathbf{x})^T \mathbf{J}_{\mathbf{g}}(\mathbf{x})) - \alpha L_g) \sum_{i=1}^n \sigma_i^2. \quad (29)$$

For the case in which $\mathbf{g}(\mathbf{x})$ is a gradient perturbed by Gaussian noise, Lemma A.2 refines L_g to a specific value $L_g = \frac{n}{\sqrt{2\pi\sigma^2}} \exp(-\frac{1}{2\sigma^2})$. \square

A.3 Proof of Theorem 5.3

Theorem 5.3 (Convergence of Attack Loss). Assume that the attack loss \mathcal{L} is α' -smooth and β' -strongly convex with respect to \mathbf{x} . When GIA is executed following Algorithm 1, the sequence $\{\mathcal{L}(\mathbf{x}_t)\}_{t=T}^0$ monotonically decreases as the denoising steps progress from timestep $t = T$ to $t = 0$.

To prove Theorem 5.3, Lemma A.3 is necessary. We omit its proof for brevity, as it is straightforward to derive.

Lemma A.3. Assume that the attack loss $\mathcal{L}(\mathbf{x})$ is α' -smooth and β' -strongly convex with respect to \mathbf{x} . Let $H(\mathcal{L}(\mathbf{x}))$ represents the Hessian of \mathcal{L} with respect to \mathbf{x} , we have:

$$\beta' I \preceq H(\mathcal{L}(\mathbf{x})) \preceq \alpha' I, \quad (30)$$

where I is the identity matrix.

Proof of Theorem 5.3. Take Taylor expansion on $\mathcal{L}(\mathbf{x})$ around \mathbf{x}_t , which states:

$$\mathcal{L}(\mathbf{x}) = \mathcal{L}(\mathbf{x}_t) + (\nabla_{\mathbf{x}} \mathcal{L}(\mathbf{x}_t))^T (\mathbf{x} - \mathbf{x}_t) + \frac{1}{2} (\mathbf{x} - \mathbf{x}_t)^T H(\mathcal{L}(\mathbf{c})) (\mathbf{x} - \mathbf{x}_t), \quad (31)$$

where \mathbf{c} is some point between \mathbf{x} and \mathbf{x}_t .

Subsequently, we have:

$$\begin{aligned} \mathcal{L}(\mathbf{x}_{t-1}) - \mathcal{L}(\mathbf{x}_t) &= (\nabla_{\mathbf{x}} \mathcal{L}(\mathbf{x}_t))^T (\mathbf{x}_{t-1} - \mathbf{x}_t) + \frac{1}{2} (\mathbf{x}_{t-1} - \mathbf{x}_t)^T H(\mathcal{L}(\mathbf{c})) (\mathbf{x}_{t-1} - \mathbf{x}_t) \\ &\leq (\nabla_{\mathbf{x}} \mathcal{L}(\mathbf{x}_t))^T (\mathbf{x}_{t-1} - \mathbf{x}_t) + \frac{\alpha'}{2} (\mathbf{x}_{t-1} - \mathbf{x}_t)^T (\mathbf{x}_{t-1} - \mathbf{x}_t). \end{aligned} \quad (32)$$

The inequality holds because the eigenvalues of $H(\mathcal{L}(\mathbf{c}))$ are bounded within $[\beta', \alpha']$. Since $\mathbf{x}_{t-1} = \arg \min_{\mathbf{x}} (\nabla_{\mathbf{x}} \mathcal{L}(\mathbf{x}_t))^T (\mathbf{x} - \mathbf{x}_t)$ where $\mathbf{x} \in S_{\mu_{\theta}(\mathbf{x}_t, t), \sqrt{n}\sigma_t}^n$, substituting any other value for \mathbf{x}_{t-1} would amplify the upper bound in Equation (32). By replacing \mathbf{x}_{t-1} with \mathbf{x}_{t-1}^+ where

$$\mathbf{x}_{t-1}^+ = \frac{(\nabla_{\mathbf{x}} \mathcal{L}(\mathbf{x}_t))^T \mathbf{x}_t - \frac{\alpha'}{2} (\mathbf{x}_{t-1} - \mathbf{x}_t)^T (\mathbf{x}_{t-1} - \mathbf{x}_t)}{(\nabla_{\mathbf{x}} \mathcal{L}(\mathbf{x}_t))^T (\nabla_{\mathbf{x}} \mathcal{L}(\mathbf{x}_t))} \cdot \nabla_{\mathbf{x}} \mathcal{L}(\mathbf{x}_t). \quad (33)$$

we have:

$$\mathcal{L}(\mathbf{x}_{t-1}) - \mathcal{L}(\mathbf{x}_t) \leq (\nabla_{\mathbf{x}} \mathcal{L}(\mathbf{x}_t))^T (\mathbf{x}_{t-1}^+ - \mathbf{x}_t) + \frac{\alpha'}{2} (\mathbf{x}_{t-1} - \mathbf{x}_t)^T (\mathbf{x}_{t-1} - \mathbf{x}_t) = 0. \quad (34)$$

\square

A.4 Proof of Theorem 5.4

Theorem 5.4 (Convergence Rate of Attack Loss). Under Assumptions 5.1-5.4, and assuming that the attack loss \mathcal{L} is α' -smooth and β' -strongly convex with respect to \mathbf{x} , if the attack loss is optimized using Algorithm 1, it satisfies:

$$\begin{aligned} \mathcal{L}(\mathbf{x}_{t-1}) - \mathcal{L}(\mathbf{x}_t) &\geq \frac{\beta' n \sigma_t^2}{2} + \beta' k \sqrt{n} \sigma_t + \frac{\beta' k^2}{2} \\ &\quad - (k + \sqrt{n} \sigma_t) (\sqrt{\lambda_{\max}(\mathbf{J}_{\mathbf{g}}(\mathbf{x}) \mathbf{J}_{\mathbf{g}}(\mathbf{x})^T)} \cdot L_g), \end{aligned}$$

where n is \mathbf{x} 's dimension, k is a positive constant, $\lambda_{\max}(\cdot)$ is the largest eigenvalue of \cdot , and $L_g = \frac{n}{\sqrt{2\pi\sigma^2}} \exp(-\frac{1}{2\sigma^2})$.

The derivation of the lower bound for the attack loss decrease rate in Theorem 5.4 leverages Lemma A.4, which establishes an upper bound for $\|\nabla_{\mathbf{x}} \mathcal{L}(\mathbf{x}_t)\|_2$.

Lemma A.4 (Upper bound of $\|\nabla_{\mathbf{x}} \mathcal{L}(\mathbf{x}_t)\|_2$). *Under conditions in Assumptions 5.1-5.4, the upper bound of $\|\nabla_{\mathbf{x}} \mathcal{L}(\mathbf{x}_t)\|_2$ is:*

$$\|\nabla_{\mathbf{x}} \mathcal{L}(\mathbf{x}_t)\|_2 \leq \sqrt{\lambda_{\max}(\mathbf{J}_{\mathbf{g}}(\mathbf{x}) \mathbf{J}_{\mathbf{g}}(\mathbf{x})^T)} \cdot L_g, \quad (35)$$

where $\mathbf{x} \in \mathbb{R}^n$, and $L_g = \frac{n}{\sqrt{2\pi\sigma^2}} \exp(-\frac{1}{2\sigma^2})$.

We begin by proving Lemma A.4.

Proof of Lemma A.4. Expanding $\|\nabla_{\mathbf{x}} \mathcal{L}(\mathbf{x})\|_2^2$:

$$\begin{aligned} \|\nabla_{\mathbf{x}} \mathcal{L}(\mathbf{x})\|_2^2 &= (\nabla_{\mathbf{x}} \mathcal{L}(\mathbf{x}))^T (\nabla_{\mathbf{x}} \mathcal{L}(\mathbf{x})) \\ &= (\mathbf{J}_{\mathbf{g}}(\mathbf{x})^T \nabla_{\mathbf{g}} \mathcal{L}(\mathbf{g}(\mathbf{x})))^T (\mathbf{J}_{\mathbf{g}}(\mathbf{x})^T \nabla_{\mathbf{g}} \mathcal{L}(\mathbf{g}(\mathbf{x}))) \\ &= \nabla_{\mathbf{g}} \mathcal{L}(\mathbf{g}(\mathbf{x}))^T (\mathbf{J}_{\mathbf{g}}(\mathbf{x}) \mathbf{J}_{\mathbf{g}}(\mathbf{x})^T) \nabla_{\mathbf{g}} \mathcal{L}(\mathbf{g}(\mathbf{x})). \end{aligned} \quad (36)$$

Assuming that the eigendecomposition of $\mathbf{J}_{\mathbf{g}}(\mathbf{x}) \mathbf{J}_{\mathbf{g}}(\mathbf{x})^T$ is $\mathbf{J}_{\mathbf{g}}(\mathbf{x}) \mathbf{J}_{\mathbf{g}}(\mathbf{x})^T = U^T \Lambda U$, then we have:

$$\begin{aligned} \|\nabla_{\mathbf{x}} \mathcal{L}(\mathbf{x})\|_2^2 &= \nabla_{\mathbf{g}} \mathcal{L}(\mathbf{g}(\mathbf{x}))^T (U^T \Lambda U) \nabla_{\mathbf{g}} \mathcal{L}(\mathbf{g}(\mathbf{x})) \\ &= \nabla_{\mathbf{g}} \mathcal{L}(\mathbf{g}(\mathbf{x}))^T (U^T \Lambda^{\frac{1}{2}} \Lambda^{\frac{1}{2}} U) \nabla_{\mathbf{g}} \mathcal{L}(\mathbf{g}(\mathbf{x})) \\ &= \nabla_{\mathbf{g}} \mathcal{L}(\mathbf{g}(\mathbf{x}))^T (U^T (\Lambda^{\frac{1}{2}})^T \Lambda^{\frac{1}{2}} U) \nabla_{\mathbf{g}} \mathcal{L}(\mathbf{g}(\mathbf{x})) \\ &= (\Lambda^{\frac{1}{2}} U \nabla_{\mathbf{g}} \mathcal{L}(\mathbf{g}(\mathbf{x})))^T (\Lambda^{\frac{1}{2}} U \nabla_{\mathbf{g}} \mathcal{L}(\mathbf{g}(\mathbf{x}))) \\ &= \|\Lambda^{\frac{1}{2}} U \nabla_{\mathbf{g}} \mathcal{L}(\mathbf{g}(\mathbf{x}))\|_2^2. \end{aligned} \quad (37)$$

Thus,

$$\begin{aligned} \|\nabla_{\mathbf{x}} \mathcal{L}(\mathbf{x})\|_2 &= \|\Lambda^{\frac{1}{2}} U \nabla_{\mathbf{g}} \mathcal{L}(\mathbf{g}(\mathbf{x}))\|_2 \\ &\leq \|\Lambda^{\frac{1}{2}}\|_2 \|U \nabla_{\mathbf{g}} \mathcal{L}(\mathbf{g}(\mathbf{x}))\|_2 = \|\Lambda^{\frac{1}{2}}\|_2 \|\nabla_{\mathbf{g}} \mathcal{L}(\mathbf{g}(\mathbf{x}))\|_2 \\ &\leq \sqrt{\lambda_{\max}(\mathbf{J}_{\mathbf{g}}(\mathbf{x}) \mathbf{J}_{\mathbf{g}}(\mathbf{x})^T)} \cdot L_g, \end{aligned} \quad (38)$$

where $L_g = \frac{n}{\sqrt{2\pi\sigma^2}} \exp(-\frac{1}{2\sigma^2})$. □

We then prove Theorem 5.4.

Proof of Theorem 5.4. According to Lemma A.3:

$$\begin{aligned} \mathcal{L}(\mathbf{x}_{t-1}) - \mathcal{L}(\mathbf{x}_t) &= (\nabla_{\mathbf{x}} \mathcal{L}(\mathbf{x}_t))^T (\mathbf{x}_{t-1} - \mathbf{x}_t) + \frac{1}{2} (\mathbf{x}_{t-1} - \mathbf{x}_t)^T H(\mathcal{L}(\mathbf{c})) (\mathbf{x}_{t-1} - \mathbf{x}_t) \\ &\geq \underbrace{(\nabla_{\mathbf{x}} \mathcal{L}(\mathbf{x}_t))^T (\mathbf{x}_{t-1} - \mathbf{x}_t)}_{(*)} + \underbrace{\frac{\beta'}{2} (\mathbf{x}_{t-1} - \mathbf{x}_t)^T (\mathbf{x}_{t-1} - \mathbf{x}_t)}_{(**)} \end{aligned} \quad (39)$$

In Equation (39), \mathbf{x}_{t-1} is defined as $\arg \min_{\mathbf{x}} (\nabla_{\mathbf{x}} \mathcal{L}(\mathbf{x}_t))^T (\mathbf{x} - \mathbf{x}_t)$ for $\mathbf{x} \in S_{\mu_{\theta}(\mathbf{x}_t, t), \sqrt{n}\sigma_t}^n$. In our specific case, we obtain $\mathbf{x}_{t-1} = \mu_{\theta}(\mathbf{x}_t, t) - \sqrt{n}\sigma_t d^*$ where $d^* = \frac{\nabla_{\mathbf{x}} \mathcal{L}(\mathbf{x}_t)}{\|\nabla_{\mathbf{x}} \mathcal{L}(\mathbf{x}_t)\|_2}$. Consequently, for (*), we have:

$$\begin{aligned}
(*) &= (\nabla_{\mathbf{x}}\mathcal{L}(\mathbf{x}_t))^T (\mathbf{x}_{t-1} - \mu_{\theta}(\mathbf{x}_t, t) + \mu_{\theta}(\mathbf{x}_t, t) - \mathbf{x}_t) \\
&= -\sqrt{n}\sigma_t \|\nabla_{\mathbf{x}}\mathcal{L}(\mathbf{x}_t)\|_2 + (\nabla_{\mathbf{x}}\mathcal{L}(\mathbf{x}_t))^T (\mu_{\theta}(\mathbf{x}_t, t) - \mathbf{x}_t).
\end{aligned} \tag{40}$$

For (**), we have:

$$\begin{aligned}
(**) &= \frac{\beta'}{2} (\mathbf{x}_{t-1} - \mathbf{x}_t)^T (\mathbf{x}_{t-1} - \mathbf{x}_t) \\
&= \frac{\beta'}{2} (\mathbf{x}_{t-1} - \mu_{\theta}(\mathbf{x}_t, t))^T (\mathbf{x}_{t-1} - \mu_{\theta}(\mathbf{x}_t, t)) \\
&\quad + \frac{\beta'}{2} (\mu_{\theta}(\mathbf{x}_t, t) - \mathbf{x}_t)^T (\mu_{\theta}(\mathbf{x}_t, t) - \mathbf{x}_t) \\
&\quad + \mu(\mathbf{x}_{t-1} - \mu_{\theta}(\mathbf{x}_t, t))^T (\mu_{\theta}(\mathbf{x}_t, t) - \mathbf{x}_t) \\
&= \frac{\beta' n \sigma_t^2}{2} + \frac{\beta'}{2} (2\mathbf{x}_{t-1} - \mathbf{x}_t - \mu_{\theta}(\mathbf{x}_t, t))^T (\mu_{\theta}(\mathbf{x}_t, t) - \mathbf{x}_t) \\
&= \frac{\beta' n \sigma_t^2}{2} + \frac{\beta'}{2} (\mathbf{x}_{t-1} - \mathbf{x}_t)^T (\mu_{\theta}(\mathbf{x}_t, t) - \mathbf{x}_t) \\
&\quad + \frac{\beta'}{2} (\mathbf{x}_{t-1} - \mu_{\theta}(\mathbf{x}_t, t))^T (\mu_{\theta}(\mathbf{x}_t, t) - \mathbf{x}_t).
\end{aligned} \tag{41}$$

To derive the lower bound of $\mathcal{L}(\mathbf{x}_{t-1}) - \mathcal{L}(\mathbf{x}_t)$, the common factor identified is $\mu_{\theta}(\mathbf{x}_t, t) - \mathbf{x}_t$. The terms $\frac{\beta'}{2} (\mathbf{x}_{t-1} - \mathbf{x}_t)^T (\mu_{\theta}(\mathbf{x}_t, t) - \mathbf{x}_t)$ and $\frac{\beta'}{2} (\mathbf{x}_{t-1} - \mu_{\theta}(\mathbf{x}_t, t))^T (\mu_{\theta}(\mathbf{x}_t, t) - \mathbf{x}_t)$ in Equation (41) represent two inner products. To demonstrate how the denoising ability can reduce the attack loss, we seek a value that is demonstrably achievable. Considering the randomness in $\mu_{\theta}(\mathbf{x}_t, t)$, by setting $\mu_{\theta}(\mathbf{x}_t, t) - \mathbf{x}_t = -kd^*$ ($k > 0$), the term $\frac{\beta'}{2} (\mathbf{x}_{t-1} - \mu_{\theta}(\mathbf{x}_t, t))^T (\mu_{\theta}(\mathbf{x}_t, t) - \mathbf{x}_t)$ in Equation (41) can be expressed as:

$$\frac{\beta'}{2} (\mathbf{x}_{t-1} - \mu_{\theta}(\mathbf{x}_t, t))^T (\mu_{\theta}(\mathbf{x}_t, t) - \mathbf{x}_t) = -\frac{\beta'}{2} (\sqrt{n}\sigma_t d^*)^T (-kd^*) = \frac{\beta' k \sqrt{n}\sigma_t}{2}. \tag{42}$$

Then, the term $\frac{\beta'}{2} (\mathbf{x}_{t-1} - \mathbf{x}_t)^T (\mu_{\theta}(\mathbf{x}_t, t) - \mathbf{x}_t)$ in Equation (41) is:

$$\begin{aligned}
&\frac{\beta'}{2} (\mathbf{x}_{t-1} - \mathbf{x}_t)^T (\mu_{\theta}(\mathbf{x}_t, t) - \mathbf{x}_t) \\
&= \frac{\beta'}{2} (\mathbf{x}_{t-1} - \mu_{\theta}(\mathbf{x}_t, t) - kd^*)^T (-kd^*) \\
&= -\frac{\beta'}{2} ((\sqrt{n}\sigma_t - k)d^*)^T (-kd^*) \\
&= \frac{\beta' k (\sqrt{n}\sigma_t + k)}{2}.
\end{aligned} \tag{43}$$

The (*) is:

$$\begin{aligned}
(*) &= -\sqrt{n}\sigma_t \|\nabla_{\mathbf{x}}\mathcal{L}(\mathbf{x}_t)\|_2 + (\nabla_{\mathbf{x}}\mathcal{L}(\mathbf{x}_t))^T (\mu_{\theta}(\mathbf{x}_t, t) - \mathbf{x}_t) \\
&= -\sqrt{n}\sigma_t \|\nabla_{\mathbf{x}}\mathcal{L}(\mathbf{x}_t)\|_2 - k \|\nabla_{\mathbf{x}}\mathcal{L}(\mathbf{x}_t)\|_2.
\end{aligned} \tag{44}$$

Finally, we have:

$$\begin{aligned}
&\mathcal{L}(\mathbf{x}_{t-1}) - \mathcal{L}(\mathbf{x}_t) \\
&\geq \frac{\beta' n \sigma_t^2}{2} + \beta' k \sqrt{n}\sigma_t - (k + \sqrt{n}\sigma_t) \|\nabla_{\mathbf{x}}\mathcal{L}(\mathbf{x}_t)\|_2 + \frac{\beta' k^2}{2} \\
&\geq \frac{\beta' n \sigma_t^2}{2} + \beta' k \sqrt{n}\sigma_t - (k + \sqrt{n}\sigma_t) (\sqrt{\lambda_{\max}(\mathbf{J}_{\mathbf{g}}(\mathbf{x})\mathbf{J}_{\mathbf{g}}(\mathbf{x})^T)} \cdot L_g) + \frac{\beta' k^2}{2}.
\end{aligned} \tag{45}$$

□

To better understand the proof, see Figure 5 for details. If $\mu_{\theta}(\mathbf{x}_t, t) - \mathbf{x}_t = -kd^*$ ($k > 0$) is not satisfied, it is the case in Figure 5(a). Due to the randomness of \mathbf{x}_{t-1} , $\mu_{\theta}(\mathbf{x}_t, t) - \mathbf{x}_t = -kd^*$ ($k > 0$) can be satisfied which is the case in Figure 5(b). In this case, $\mathcal{L}(\mathbf{x}_{t-1}) - \mathcal{L}(\mathbf{x}_t)$ reaches its lower bound.

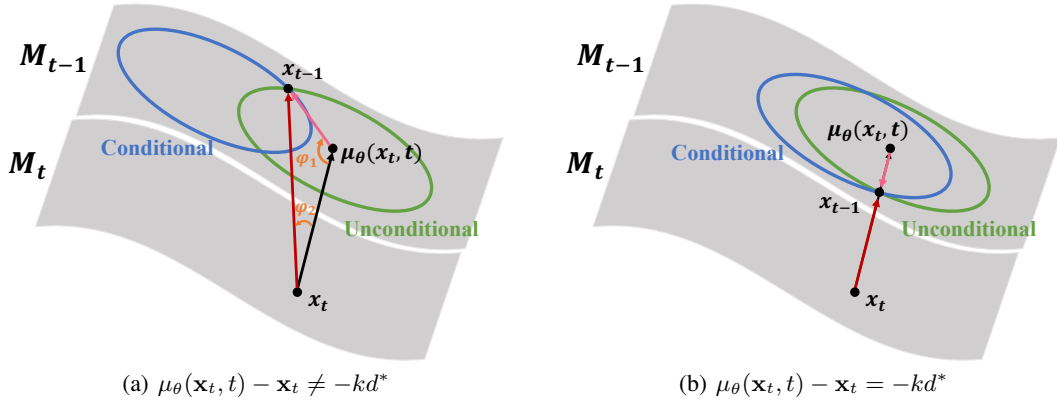


Figure 5: Explanations for Theorem 5.4.

B Additional Experimental Settings

B.1 Machine Configuration

All experiments were performed on a server equipped with dual Intel(R) Xeon(R) Silver 4310 CPUs @2.10GHz and a single A100 GPU. We implement our attack with Pytorch 2.0.1.

B.2 Architectures of Attacked Models

The architectures of attacked models are detailed as follows:

- *MLP-3/4/5*. These three Multilayer Perceptrons process flattened image inputs and utilize ReLU activations in their hidden layers. MLP-3 is a three-layer network with two hidden layers (512 and 128 units). MLP-4 extends this with three hidden layers (512, 256, and 64 units). MLP-5 further deepens the architecture, featuring four hidden layers (1028, 512, 256, and 64 units). All MLP models conclude with a linear output layer for classification.

- *CNN*. The CNN architecture consists of two convolutional layers (64 and 128 output channels, respectively, with 3×3 kernels and padding), each followed by ReLU activation and 2×2 max-pooling. Feature maps are then flattened and processed by a 256-unit ReLU fully connected layer, culminating in a softmax output for classification. This CNN serves as the default attacked model in our experiments.

- *ResNet18*. ResNet18 employs residual blocks with skip connections. It begins with an 7×7 convolutional layer and max-pooling, followed by four stages, each containing two residual blocks. Each block utilizes two 3×3 convolutional layers, batch normalization, and ReLU activation. The network concludes with adaptive average pooling and a fully connected output layer for classification.

- *VGGNet16*. Our VGGNet16 implementation adheres to the classic architecture, featuring five convolutional blocks. The initial two blocks each contain two 3×3 convolutional layers, and the subsequent blocks employ three 3×3 convolutional layers. All convolutional layers are followed by ReLU activations and 2×2 max-pooling. Flattened features then pass through a fully connected classifier with two 4096-unit ReLU layers (with dropout) and a final softmax output.

C Running Time and GPU Usage

Table 8 provides an overview of the computational resources consumed during the reconstruction process. Specifically, it details the average running time (in seconds) per conditional reverse step for GSS-R when applied to various attacked model architectures. Furthermore, the table presents the peak GPU usage (in MiB) observed throughout the reconstruction process.

Attacked Model	Running Time (s) / step	Peak GPU Usage (MiB)
ResNet18	0.2259	3396
MLP-5	2.6473	9680
VGGNet16	6.3582	30314
CNN	2.3947	7822
MLP-4	1.9149	6084
MLP-3	1.4939	5247

Table 8: Average running time (s) per gradient-guided reverse diffusion sampling step and peak GPU usage (MiB) for GSS-R.